We are IntechOpen, the world's leading publisher of Open Access books Built by scientists, for scientists

4,800
Open access books available

122,000
International authors and editors

135M
Downloads

Our authors are among the

154
Countries delivered to

TOP 1%
most cited scientists

12.2%
Contributors from top 500 universities

WEB OF SCIENCE™

Selection of our books indexed in the Book Citation Index in Web of Science™ Core Collection (BKCI)

Interested in publishing with us?
Contact book.department@intechopen.com

Numbers displayed above are based on latest data collected.
For more information visit www.intechopen.com

11

Steady-state and Time-dependent LPP Modeling

White, Dunne, and O'Sullivan
University College Dublin
Ireland

1. Introduction

A primary goal in developing extreme ultraviolet lithography (EUVL) is the modeling of plasma-based light sources, created either by intense lasers or high-current pulsed discharges, which have applications in semiconductor lithography, nanotechnology, and plasma diagnostics (Attwood, 2004, Derra et al., 2005). Such modeling can be the key factor to important scientific and technological solutions in EUVL source optimization. Radiation hydrodynamic modeling is also important in astrophysics and inertial confinement fusion.

As stated in the *International Technology Roadmap for Semiconductors* (2008), "Extreme ultraviolet lithography is expected to provide a single exposure solution for use in manufacturing starting at 22 nm half pitch and possibly for 32 nm half pitch." To match the proposed multilayer Mo/Si mirror imaging system (~70% refelctivity at 13.5 nm), the EUVL wavelength of choice for high-density, low-cost integrated circuits is 13.5 nm, created either by a tin containing laser-produced plasma (LPP) or discharge produced plasma (DPP). The source power must be greater than 180 W at intermediate focus.

In-band EUV emission (13.365–13.635 nm) in a range of overlapping tin ions (Sn^{4+} to Sn^{13+}) has previously been identified as originating from 4d-4f, 4p-4d, and 4d-5p transitions (O'Sullivan & Carroll, 1981). The source conditions for optimum brightness are in the computationally challenging non-local thermodynamic equilibrium (non-LTE) (*a.k.a.* collisional-radiative or CR) regime, and the emission is highly anisotropic in spectral shape and intensity (Hayden et al., 2006) for all DPPs and most LPPs (i.e., slab or liquid jet targets). Xenon and lithium sources have been proposed as possible targets, but are no longer considered viable (Al-Rabban et al., 2005).

There are numerous challenges to develop and integrate efficient and cost-effective high-flux plasma EUV sources; in particular the improved conversion efficiency (CE) (ratio of 13.5 nm in-band emission to input laser energy) of the proposed source, and the characterization and mitigation of debris (fast ions, neutrals, and nanoparticles). Of primary importance is to identify optimum source parameters (laser wavelength, λ, pulse duration, τ, power density, Φ, and pulse shape) and material composition (e.g., target shape and ion concentration) for maximum CE, particularly with the use of reliable modeling tools.

Laser-plasma interaction is complex, but the fundamentals are as follows. A laser is incident on a target, producing an ablation front, an over-dense region up to 10^3 times solid, which creates a shockwave in the target as well as heating and ionizing the target to produce an

Source: Lithography, Book edited by: Michael Wang,
ISBN 978-953-307-064-3, pp. 656, February 2010, INTECH, Croatia, downloaded from SCIYO.COM

expanding plasma, a process that continues throughout the pulse duration. Photons are absorbed by inverse Bremsstrahlung, and re-emitted via recombination, where up to 80% of the incident energy can be converted to EUV radiation. The plasma expands (typical ion velocities are up to 10^6 cm/s) but as electron density decreases, less laser energy is absorbed. The plasma is a self-regulating regime of generation, heating, and expansion over the pulse duration, where electrons equilibriate on a very small time scale compared to pulse duration. Opacity effects are important since emitted radiation can be significantly reabsorbed within the plasma. A wide range of electron densities and temperatures exist, which require challenging atomic and plasma hydrodynamic models (Greim, 1964, Key & Hutcheon, 1980, Carroll & Kennedy, 1981, Attwood, 1999, Al-Rabban et al., 2005).
Section 2 presents a background survey of some typical LPP models, citing conditions for optimum emission where possible. Major issues in modeling steady-state and time-dependent plasmas are discussed in Section 3. Firstly, a straightforward steady-state model in the optically thin regime (emitted radiation not reabsorbed) is used, which provides a simple estimation of optimum electron temperature at maximum in-band emission, from which important information about the complex atomic physics in LPPs can be determined. Secondly, a more sophisticated 1D model that includes radiation transport within an optically thick plasma (emitted radiation reabsorbed) is used, from which the conversion efficiency using different laser parameters can be calculated. Some 2D results are also presented which take into account lateral expansion. Section 4 presents current trends and future challenges in the field of LPP modeling and EUV source optimisation.

2. Modeling background

To give a background to LPP modeling, a number of cases are cited that highlight a variety of codes, laser parameters (wavelength, pulse duration, power density), target material and geometry, and dimension, as well as recent results related specifically to EUVL. The choice is by no means exhaustive, but is intended to give an idea of the different approaches to optimising LPP parameters. For brevity, nomenclature is used without introduction, but can be found in Section 3. Note that the following survey is intended as background only and the reader is directed to the literature for more detail.
Atomic structure codes such as the HFCI (Hartree Fock with Configuration Interaction) code of Cowan (Cowan, 1981), GRASP (Grant et al., 1980), HULLAC (Bar-Shalom et al., 2001), and FAC (Gu, 2003), among others, have been used to determine cross sections and transitions involved in spectral emission. A number of plasma codes exist to model hydrodynamics, such as the steady-state, 0D, CR code of Colombant & Tonon (1973), the 1D Lagrangian code MEDUSA (Christiansen et al., 1974) and the 2D codes CASTOR (Christiansen & Winsor, 1979), LASNEX (Zimmerman & Kruer, 1975) and Z* (Zakharov et al., 2005), which all use a simplified single electron model that excludes detailed atomic term structure. These codes are discussed more fully as applicable below.
The postprocessor FLY code (Lee, 1995) is a time-dependent, single-cell, hydro-dynamics, CR-based model that solves the differential rate equation using a 1st-order escape probability approximation, valid for photons that are absorbed locally or escape without interactions. SWARM (Sondhauss et al., 2001) is a multi-cell extension to FLY using the Average Atom (AA) model which accounts for non-local re-absorption in the plasma. Angle-resolved spectra can be calculated for planar, cylindrical, or spherical target geometries that account for Doppler-shifted anisotropic radiation. FLYCHK is an online

extension to FLY which incorporates HULLAC atomic data for non-H-, He-, and Li-like plasmas (Chung et al., 2005). However, accuracy is limited as the AA model is essentially a Bohr atom approach and ion level energies are assumed to be *l*-degenerate, a major drawback when dealing with medium to high Z species such as Sn.

SCROLL (Bar-Shalom, 1997) is a super configuration, non-LTE CR model, which modifies a simpler LTE model by splitting supershells to populate new superconfigurations proportional to their partition function (> 10^{-5} of total population). Levels up to n = 8 were considered in optically thin selenium (Z = 34) and lutetium (Z = 71) plasmas.

To account for *nl*-splitting, the atomic model of Mirone et al. (1997) assumes thermodynamic equilibrium for population levels using the AA, screened-charge model (a reasonable assumption where collisions are dominant) to reconstruct the one-electron atomic potentials. The authors also used the LTE hydrodynamic code MULTI (λ = 0.53-μm, τ = 0.5-ns, 3-μm diameter germanium target) to highlight the effect of radiation loss in non-LTE conditions. Their simulations showed that a non-LTE plasma model produces a hotter corona, reduced radiative heat wave, and more penetration than in an LTE plasma, though less so with their reconstructed versus hydrogenic model.

The kinematics of supersonic ionization fronts and radiation transport was studied in Gumbrell et al. (1998) for ps-pulses, where measured plasma velocities are up to 40 times greater than for ns-pulses. A 1D laser-plasma hydrodynamics code based on MEDUSA was used to describe heating within the target.

Dürsterer et al. (2001) conducted experiments on oxygen-containing targets (Nd:YAG, 700-mJ, τ = 8-ns, ~10-μm diameter mass-limited water droplets and 20-μm diameter solid glass SiO_2 spheres). The authors noted that laser energy absorption is always less than 100% but is insufficient for pulses of either too short or too long duration: for shorter pulses, absorption is reduced; for longer pulses, greater expansion reduces electron density below critical (where the trailing edge of a long pulse is not absorbed at all). They noted a logarithmic increase in CE over 5 orders of magnitude of pulse duration (200 fs–6 ns), and that energy was independent of pulse duration for a finite drop for optimum EUV emission because of the fixed number of atoms. They also noted that a mass-limited droplet expands much faster and isotropically in 3D compared to an essentially 1D expansion in a bulk target, and suggested that energy and pulse duration be independently optimized in mass-limited targets rather than intensity (sufficient for bulk targets). Using a steady-state CR model they found the optimum electron temperature was 30 eV (reasonably agreeing with a blackbody model of 95 eV). From MEDUSA simulations, they noted that spherical targets cool faster and that the position of critical density moves slower than in bulk targets.

Sasaki et al. (2004) use the parametric potential atomic code HULLAC and CR Whiam code to calculate Xe and Sn emission spectra. The authors assume LTE and a spherical plasma to simplify the rate equations. For xenon, a calculated spectrum (n_e = 10^{21} cm^{-3} at T_e = 25 eV) is compared to experiment (Nd:YAG, τ = 8-ns, Φ = 10^{12} W/cm^2, gas jet target), and for tin, a calculated spectrum (n_e = 10^{20} cm^{-3} at T_e = 22 eV, uniform sphere of radius 30 μm) is compared to experiment (Φ = 1–9.6 10^{11} W/cm^2). The authors note the effect of satellite lines in sufficiently dense plasmas (on the long wavelength side of the UTA) and the considerable opacity effects in a higher density plasma. They also included configuration interaction (CI) effects to describe the atomic physics in both HULLAC and GRASP. They comment that a plasma is in quasi-steady-state if the temporal evolution of the EUV spectral intensity is identical to the input laser pulse shape.

Fujioka et al. (2005) used a 6-beam, Gekko II laser (λ = 1.053-μm, τ = 5-ns, Φ = 1 x 10^{13} W/cm^2), and observed that the expansion velocity of 3.8 x 10^6 cm/s compared well with that predicted by ILESTA-1D. The authors noted that the calculated UTA width was broader than the experimental UTA width (see also Mandelbaum et al. (1997)). Simple modeling using just *gA* or *f*-value distributions for reproducing spectra based on the assumption that levels are populated uniformly within a particular configuration does not take into account the energy dependence of the excitation rate coefficients which strongly influence the UTA shape, however, and accurate term specific rate coefficients are essential for very accurate modeling. The atomic physics was modelled using HULLAC with CI included, although the authors noted that disagreements between experimental and calculated spectra result from the number of configurations used. They noted that opacity effects are a function of plasma size, and that there are two well-known ways to change plasma size: 1) by incident wavelength—a shorter wavelength heats higher density regions producing a larger plasma, 2) by pulse duration—a longer duration produces a larger plasma. They also noted that satellite emission originated from deeper (higher density) layers than the UTA emission. The experimental CE versus power density was shown to be qualitatively consistent with their calculated CE (using the 1D code STAR and HULLAC), and that a shorter pulse duration leads to a higher CE.

Tao et al. (2005) conducted a comparison between experiment (λ = 1.064-μm, τ =10-ns, 220-μm focal spot diameter, Φ = 0.1-3 x 10^{11} W/cm^2 at normal incidence) and a 1D simulation (Φ = 1 x 10^{11} W/cm^2), which showed reasonable agreement, noting that the difference was because of lateral expansion not accounted for in the 1D code. The authors noted that because of a finite focal spot size, which was comparable to the plasma size, lateral expansion occurs, which removes plasma energy, reduces ion velocity, and reduces ion density. They commented that due to opacity effects, most of the EUV radiation comes from the under-dense, coronal region, which they observed using two interferometers and two probe beams (at 266 nm and 532 nm) to profile electron density along the centre of the plasma. They observed that at Φ = 1 x 10^{11} W/cm^2 the electron temperature in the coronal region is close to optimum value, whereas at higher intensities it is too hot.

Yamaura et al. (2005) used the 12-beam Gekko XII facility (Nd:YAG, λ = 1064-nm and 4ω 266-nm, τ= 6.5-ns and 10-ns, spatial flattop, Φ = 10^{10}-10^{11} W/cm^2 at normal incidence, tin target) and large spot sizes (~500 μm) to exclude the effect of energy loss from lateral expansion. The authors reported an absorption dip at 13.5 nm for the 266-nm wavelength due to greater opacity in the lower-wavelength, higher-density plasma, which was reproduced in a 1D code. They also noted an angular dependence of $\cos^{1.3}\theta$ at 266 nm and $\cos^{0.5}\theta$ at 1064 nm, and reported that the shifted-peak 4ω spectrum (to 13 nm) could be used with a modified Mo/Si mirror system.

Shimada et al. (2005) used the 12-beam Gekko XII laser (τ =1.2-ns, target diameter varied from 300-700-μm, Φ = 0.2–1 x 10^{11} W/cm^2, dodecahedral configuration), primarily used in fusion research, to uniformly irradiate a spherical tin target and thus remove 2D effects to compare with a 1D code. Using a EUV pinhole camera, they observed that the diameter of emission expanded to several tens of microns. They noted that at Φ = 1.2 x 10^{11} W/cm^2, the temporal EUV profile precisely matched the laser profile, whereas at Φ = 9.6 x 10^{11} W/cm^2, the spectral maximum occurred much later during the delayed recombination phase. A maximum CE of 3% occurred at Φ = 0.5–1 x 10^{11} W/cm^2.

MacFarlane et al. (2005) used the 1D Lagrangian code HELIOS-CR and postprocessor SPECT3D to study LPPs and z-pinches. The material equations of state are based on SESAME or PROPACEOS tables and frequency-dependent opacities on non-LTE level populations. Atomic cross sections were calculated using ATBASE and oscillator strengths from a HFCI model, where in Sn^{10+}, for example, ~500 higher *n*-shell configurations (to n = 9) and 57 doubly excited configurations were included. More than 5 x 10^6 oscillator strengths and energy levels from Sn I to Sn XX were computed. In planar geometry, radiation is transmitted along a single ray at an angle θ with incidence, and in spherical geometry along a multi-ray conical path. The authors compared HELIOS-CR output to data from the 12-beam Gekko XII (λ = 1.06-μm, τ = 1.2-ns, Φ = 0.9–9 x 10^{11} W/cm^2, 700-μm diameter CH spheres coated with a 1-μm tin layer), which showed good agreement with tin UTA evolution. Planar tin foil experiments were also conducted (λ = 1.06-μm & τ = 1-ns, λ = 0.35-μm & τ = 10-ns) giving a maximum CE of 4.5% for the 1.06-μm & 1-ns case. They also noted that CEs were higher for targets in front of the laser focus because the plasma couples to a larger effective laser spot size as it expands outward.

Zakarov et al. (2005) used the 2D RMHD Z* to model EUV spectra in a number of scenarios, the preprocessing code THERMOS to calculate the spectral and plasma transport coefficients and material and mixtures EOS database, and the postprocessor code RAY which includes the effect of complex level kinetics. Z* results (λ = 1064-nm, τ = 15-ns, flat pulse, 30–300-mJ, 40-μm diameter focussed spot on a 30-μm diameter solid Sn or cryogenic Xe droplet) showed a CE of about 3% for tin and 0.65% for xenon. The authors noted that the total emission solid angle is less than 4π because of the target shadow, and that the plasma is in the shape of a conical shell, which consists of hotspots. Further pre-pulse-pulse simulations (Zakarov et al., 2007) (Nd:YAG: 2.5-mJ & τ = 10-ns pre-pulse; CO_2: 50-mJ & τ = 15-ns pulse; on 20-μm Sn droplet) at varying delay times (25–125 ns), showed CE as a function of delay time, CO_2 pulse duration and energy (τ = 20–100 ns, 20–200 mJ), and CO_2 intensity (Φ = 0.03–2 x 10^{11} W/cm^2).

The Laser Plasma Laboratory at the University of Central Florida (Al-Rabban, 2005) modelled oxygen (liquid water droplets) in spherical geometry using MED103 (λ = 1064-nm, τ = 10-ns, 80-μm spot size, Φ = 4.5 x 10^{11} W/cm^2), which predicted a maximum electron temperature of 56 eV. Line emission was modelled using the LTE code Spectra and atomic data from the astrophysical Opacity Project database (Z = 1 to 26), which produces synthetic spectra from 1 to 1000 nm. The authors also used the CHIVAS hydrodynamic code and a CR ionization model to model xenon droplets, where results showed that "important droplet expansion occurs at the beginning of the laser pulse, which results in a rather inefficient overall coupling between the laser and the spray."

Ando et al. (2006) derived a scaling law for absorption, showing that optical depth is a function of laser wavelength, pulse duration, and power density. The authors calculated that a 3–7-ns duration pulse produces an optical depth of 1 cm for a λ = 1064-nm, Φ = 1 x 10^{11} W/cm^2 laser. Their experiments (Nd:YAG, λ = 1064-nm, τ = 2–9-ns (Pockels cell), τ = 1–2-ns (SBS pulse compressor), 300–900-μm spot size with 100-nm Sn layer, Φ =0.1–10 x 10^{11} W/cm^2) showed that the EUV emitting region is thinner for shorter pulses, and that emitted EUV intensity increases as pulse duration decreases (8.5 to 2.3 ns) but decreases beyond that (to 1.2 ns). A maximum CE of 2.2% at 2.3 ns and Φ = 5.0 x 10^{11} W/cm^2 was observed. They also noted that an absorption dip at 13.5-nm decreases as the pulse duration decreases, and that the electron temperature was lower for shorter pulses due to lower absorption.

Rollinger et al. (2008) used the 2D axisymmetric hydrodynamic code POLLUX (which incorporates the steady-state CR code of Colombant & Tonon) and the atomic code HULLAC to determine ion level populations and spectra (as well as assess the limits of LTE). The authors noted that 1D codes such as MED103 misrepresent electron temperature and that non-LTE calculations lower the plasma temperature for optimum CE by 3 eV. 2D target simulations (Nd:YAG, τ =1–15-ns, Φ = 0.1–30 x 10^{11} W/cm^2, 40-μm focal spot size, 50-μm thick planar Sn target) showed that optimum CE occurs for 3–10 x 10^{11} W/cm^2, noting that power density primarily determines the electron temperature and thus effects CE more than pulse duration. They noted that a longer pulse duration produces a larger plume, which reduces CE because of heat transfer from the hotter core. They also noted that spherical targets produce lower velocities and a reduced though more 2D plume.

A number of recent experimental results have been reported that have not yet been fully modelled, but are important with regards to current trends and future challenges in modeling (see also Section 4). Ueno et al. (2008) noted a 4% CE for a CO_2 laser incident on a tin cavity target (200 μm). Fujioka et al. (2008a) noted that the target size should equal the laser spot size to suppress OOB radiation and that debris is reduced by using mass-limited targets. Sequoia et al. (2008) noted dips in the angular distribution of the in-band EUV emission at 0° and 30°, which they attributed to 2D plasma expansion. They also noted that lateral and longitudinal expansion are of similar scale for smaller spot sizes but that expansion is entirely longitudinal for larger spot sizes (more than a few hundred microns) and suggested that for higher CE, small focal spot sizes are required to match the target size.

Takahashi et al. (2008) compared the kinetic energy and particle emission for CO_2 and Nd:YAG lasers at the same energy (50 mJ), observing that the CO_2 laser produces higher ion kinetic energy (~ 4x) but lower particle emission (1/4) than the Nd:YAG. They commented that the CO_2 laser was not considered in earlier EUVL research because the deposited energy was considered too small, but noted that the dominant absorption process for longer-wavelength lasers is Joule heating ($\propto \lambda^2$) and that once the plasma has formed energy is absorbed in the plasma surface for a CO_2 laser rather than the target surface, in contrast to the more penetrating Nd:YAG.

Fujioka et al. (2008b) observed the effect of laser spot size and microdroplet diameter in pre-pulse-pulse experiments (Nd:YAG pre-pulse, τ = 8-ns, Φ = 3 x 10^{11} W/cm^2, 50-μm focal spot size, CO_2 main pulse, τ = 40-ns, 1 x 10^{10} W/cm^2, 250-μm focal spot diameter, with optimum delay of 1 μs) and observed a 4% CE (greater than the 2.5% observed from a single CO_2 pulse on a planar Sn target). They noted that the 20-μm minimum-mass droplet was too small for optimum laser coupling with the Nd:YAG pre-pulse but was sufficiently expanded prior to the CO_2 main pulse. They noted that in a 1D simulation of a single CO_2 pulse that about one half of the incident energy is reflected by the Sn plasma surface and that a pre-pulse forms a low-density, expanded target which enhances absorption. They also noted that about 1/3 of the emitted EUV radiation reaches IF, and thus 3 times the IF power is required at source (545 W into 2π).

In summary, therefore, maximum CEs in the range of 3-4% are predicted for Nd:YAG lasers operating at power densities of ~ 10^{11} W/cm^2 with pulse durations of a few ns, while for CO_2 systems, because of reduced opacities, higher CEs should be obtainable, this time in the ~ 10^{10} W/cm^2 range.

3. Major Issues

In this chapter, the theoretical analysis and computational methods used to design and create a LPP light source at 13.5 nm are discussed, with emphasis on tin as the source target. The Hartree-Fock configuration interaction (HFCI) Cowan code (Cowan, 1981), which calculates transitions between atomic configurations, and the laser parameters and resultant plasma conditions needed to produce a tuned LPP light source (O'Sullivan & Faulkner, 1995), are investigated. Unresolved transition array (UTA) statistics are calculated to characterise spectra, which result from hundreds of thousands of unresolved in-band (13.5 nm ±1%) transitions from a range of tin ions (White et al., 2005).
A steady-state model (Colombant & Tonon, 1973) is presented, which characterises the plasma by electron temperature, electron density, and average charge state (or ion stage distribution) from input parameters of laser wavelength, pulse duration, and power density. To quantify in-band emission, a source metric is presented, which convolves the in-band emission with ion densities and mirror reflectivity.
Time-dependent, spatially resolved plasmas are analysed with a 1D, hydrodynamic, laser-plasma interaction code MED103 (Christiansen et al., 1974), where level populations are calculated using an energy functional method (White et al., 2007). A radiation transport model for optically thick plasmas is presented to determine the conversion efficiency of laser energy into useable EUV radiation (Eq. 1).

$$CE = \pi \int_{13.5-1\%}^{13.5+1\%} \int_{0}^{\tau} I_{out}(\lambda, t) dt d\lambda dA / E_{tot} \tag{1}$$

where I_{out} is the emitted spectral output and E_{tot} is the input laser energy.
The effect of laser pulse wavelength (Nd:YAG λ = 1.064 μm and CO_2 λ = 10.6 μm) especially with respect to the opacity of the plasma is calculated using the 1D model and the anisotropic nature of the plasma using 2D simulations.

3.1 Atomic physics

Bauche & Bauche-Arnoult (1988a) reported that a transition array is "the totality of lines between the levels of two electronic configurations." Peyrusse (1999) reported that broadband line emission features are present in plasma emission for mid- to high-Z elements and Jin & Richardson (1995) that "high-Z solid targets, for example, those elements in the vicinity of tin, characteristically emit broadband spectra that come from many excited levels. These energy levels are so close that the radiation they generate in the EUV range can be considered a continuum." Salzmann (1998) noted that as the number of bound electrons increases, the density of lines increases such that "their spacing is smaller than their width."
In a tin plasma, hundreds of thousands of 4d-4f, 4p-4d, and 4p-5d transitions, from near-degenerate $4p^6 4d^{N-1} 4f^1 + 4p^5 4d^{N+1}$, and $4p^6 4d^{N-1} 5p^1$ (N = 9-1) excited energy levels in Sn^{5+}–Sn^{13+} ions, overlap to form a UTA in the in-band EUVL region (O'Sullivan & Carroll, 1981). To aid the computationally prohibitive calculations, UTAs can be treated statistically, using moments of the weighted oscillator strength (gf) versus wavelength (λ) distribution. The statistical approach is relevant because of the extreme complexity of the UTA features (Bauche & Bauche-Arnoult, 1992).
The HFCI Cowan code (Cowan, 1981) solves the multi-electron Schrödinger equation using the Slater-Condon theory of atomic structure. Configuration interaction (CI) effects are

known to be considerable between $4p^6 4d^{N-1} 4f$ and $4d^5 4d^{N+1}$ configurations and must be included. The *gf* versus λ distribution is shown in Figure 1, from the HFCI Cowan code for tin ions in the 12.5–14.5-nm (7.4%) range (the full Mo/Si mirror response region).

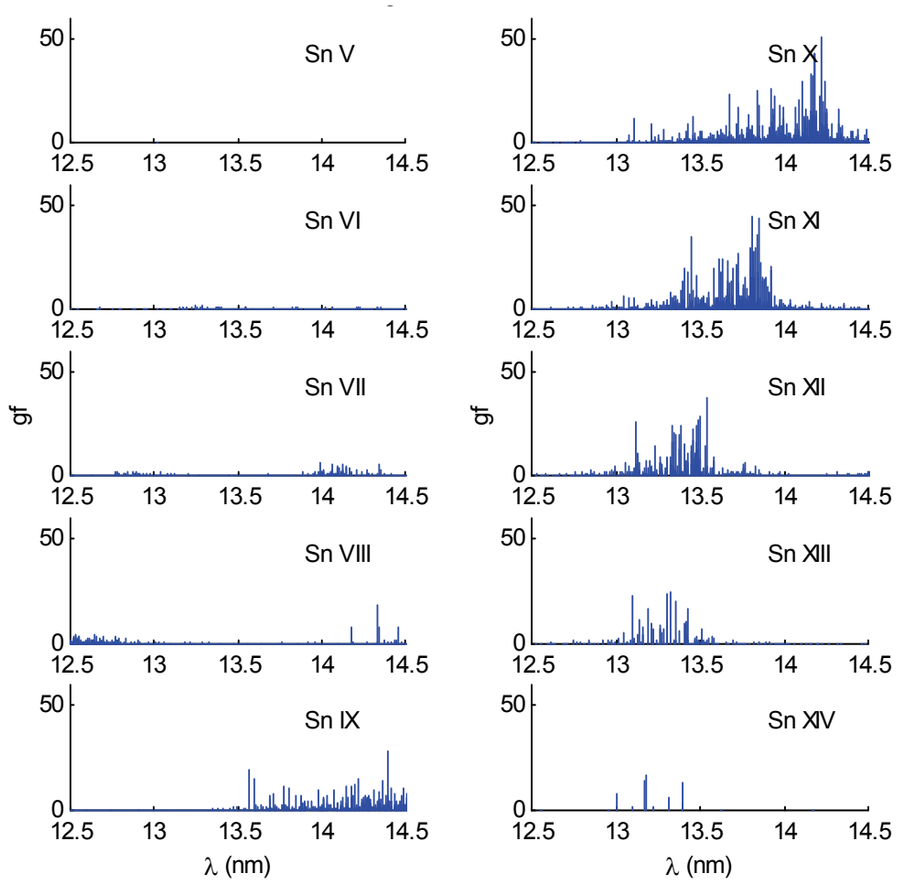

Fig. 1. Sn V–Sn XIV weighted oscillator strength versus wavelength (12.5–14.5 nm)

The statistical parameters used to describe a UTA are the weighted mean, μ_1, variance, v, skewness, α_3, and kurtosis, α_4, determined from the nth-order centred moments of the distribution (moments about the mean), $\mu_n{}^c$ (Bauche & Bauche-Arnoult, 1992). Eq. 2 gives the nth-order, non-centred moments, expressed by Q_i, the energy difference between two levels, and w_i, the strength of line i (Eq. 3).

$$\mu_n = \frac{\sum_{i=1}^{N} (Q_i)^n w_i}{\sum_{i=1}^{N} w_i} \tag{2}$$

$$w_i = \left| \left\langle \alpha J \left| \mathrm{D}^{(1)} \right| \alpha' J' \right\rangle \right|^2 \tag{3}$$

where $\mathbf{D}^{(1)}$ is the electric dipole operator and αJ and $\alpha' J'$ are the upper and lower levels.

The non-centred moments can be expressed in terms of the energy E_i (or wavelength, λ_i) and weighted oscillator strength, gf_i, for each line i (Svendsen & O'Sullivan, 1994) (Eq. 4). The gf values are used instead of intensities, assuming that the populations in the upper level are proportional to the statistical weight 2J + 1 (Bauche & Bauche-Arnoult, 1988b). The non-centred moments are centred, from which the UTA statistics are calculated.

$$\mu_n = \frac{\sum_{i=1}^{N} (\lambda_i)^n gf_i}{\sum_{i=1}^{N} gf_i} \tag{4}$$

Skewness is positive ($\alpha_3 > 0$) when the distribution is biased towards the right tail (lower energy or longer wavelength, in this case) and negative towards the left tail (higher energy or shorter wavelength). Kurtosis compares the distribution to a Gaussian (or normal) distribution, where $\alpha_4 = 3$ for a perfect Gaussian. The full width at half maximum (FWHM) instead of the variance can also be used as a measure of width (Eq. 5) as can the standard deviation, σ, the square root of the variance.

$$FWHM = \Gamma = 2\sqrt{2\log(2)}\sigma = 2.35\sigma \tag{5}$$

A UTA can thus be represented as a Gaussian by spectral position and width, in terms of the mean (μ_1) and standard deviation (σ) (Eq. 6), and convolved with an area Gaussian equal to the Σgf to produce a plot of relative intensity versus wavelength for a given ion stage. The UTA statistics from a full HFCI calculation can be calculated for each transition type based on the leading eigenvalue percentages (White et al., 2005).

$$f(x) = \frac{1}{\sigma\sqrt{2\pi}} e^{-\frac{(x-\mu_1)^2}{2\sigma^2}} \tag{6}$$

Statistical data from the Cowan code for the 4d-4f, 4p-4d, and 4d-5p transitions are given in Table 1 and the corresponding Gaussian representation in Figure 2, showing how the Gaussian representation can be used to greatly simplify complex UTA data.
Figure 3 shows the mean wavelength versus ion stage (error bars as standard deviation) for the 4d-4f, 4p-4d and 4d-5p transitions, where it is seen that the mean wavelength decreases with ionisation because of increased Coulombic force, as is to be expected. Note that $\Delta n = 0$ transitions are less sensitive than $\Delta n = 1$ transitions to the change in average nuclear charge and that the 4d-5p transition array overlaps with the 4d-4f and 4p-4d UTA in the 13.5-nm region at Sn XIII.

3.2 Steady-state ion distribution

Transition array statistics simplify numerical calculations involving hundreds of thousands of spectral lines to help interpret unresolved LPP EUV spectra. The results can be coupled with a steady-state, CR plasma model (1 electron temperature, 1 electron density) (Colombant & Tonon, 1973) to quantify in-band emission in an optically thin plasma or with a time-dependent hydrodynamic model to calculate CE for an optically thick plasma.

Ion	# lines	Σgf	mean λ (nm)	std (nm)	skew	kurt
Sn V	3	2.63	22.61	0.21	5.54	32.55
Sn VI	81	30.43	19.49	0.47	1.92	7.11
Sn VII	721	185.54	17.40	0.61	2.22	8.22
Sn VIII	2825	614.63	15.77	0.62	3.01	15.22
Sn IX	5470	1032.42	14.84	0.64	4.32	26.44
Sn X	5346	1227.41	14.34	0.70	4.17	20.50
Sn XI	2825	940.50	13.87	0.46	4.81	29.68
Sn XII	721	483.43	13.50	0.32	6.21	62.43
Sn XIII	81	129.50	13.36	0.29	8.54	93.94
Sn XIV	3	13.03	13.41	0.22	10.68	115.16

Table 1a. 4d-4f UTA statistics

Ion	# lines	Σgf	mean λ (nm)	std (nm)	skew	kurt
Sn V	0					
Sn VI	3	2.88	15.37	2.28	0.15	1.03
Sn VII	60	75.20	16.36	0.47	-0.06	2.76
Sn VIII	466	362.98	15.05	0.65	2.22	12.26
Sn IX	1718	904.94	14.30	0.59	3.50	27.04
Sn X	3170	1061.48	13.91	0.64	4.62	34.12
Sn XI	3245	888.11	13.64	0.61	4.67	33.33
Sn XII	1718	471.46	13.39	0.59	5.41	38.80
Sn XIII	466	158.26	13.34	0.69	4.61	26.41
Sn XIV	60	53.95	13.29	0.61	5.15	30.24

Table 1b. 4p-4d UTA statistics

Ion	# lines	Σgf	mean λ (nm)	std (nm)	skew	kurt
Sn V	1	0				
Sn VI	60	10.46	30.19	0.72	-0.97	7.72
Sn VII	466	44.24	25.80	0.70	-0.46	5.68
Sn VIII	1718	107.17	22.48	0.63	-0.14	5.14
Sn IX	3245	158.89	19.90	0.53	0.06	5.46
Sn X	3170	129.21	17.80	0.46	0.13	5.90
Sn XI	1718	97.46	16.07	0.41	-0.42	9.02
Sn XII	466	59.19	14.64	0.33	-0.24	6.49
Sn XIII	60	54.73	13.41	0.17	1.36	10.56
Sn XIV	3	1.05	12.43	0.10	-0.27	3.01

Table 1c. 4d-5p UTA statistics

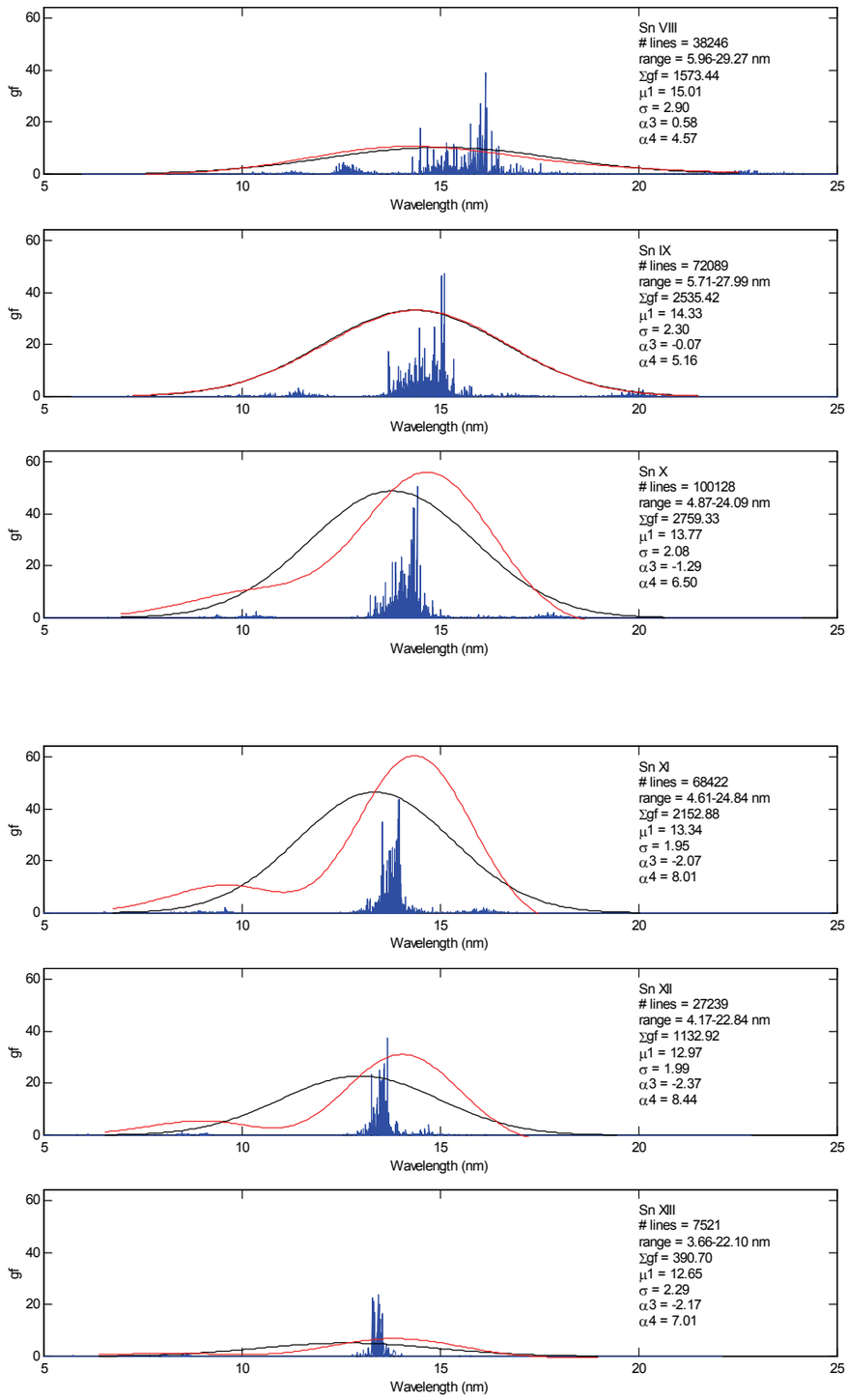

Fig. 2. Calculated discrete Cowan (blue), Gaussian (black), and skewed Gaussian (red) (Sn VIII–Sn XIII)

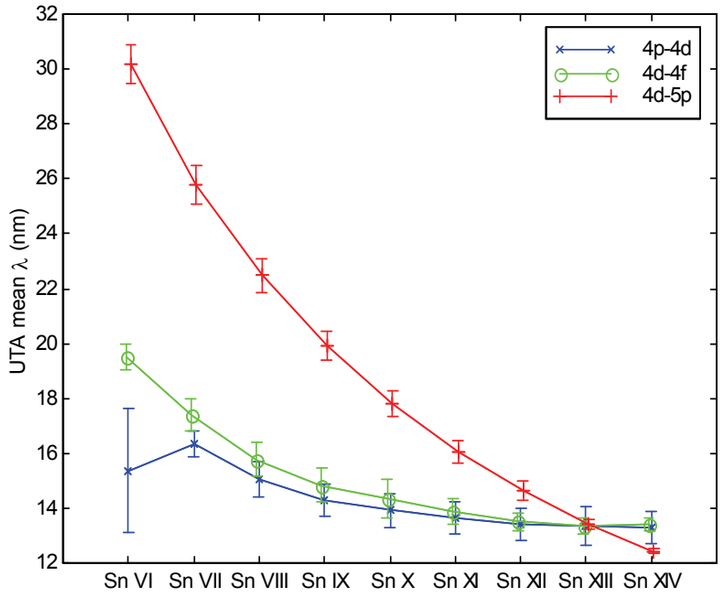

Fig. 3. 4d-4f, 4p-4d, and 4d-5p transitions arrays: mean wavelength versus ion stage

In the steady-state, CR model, collisional and radiative process for each ion state are balanced according to the rate equations for optically thin plasmas (Eq. 7).

$$\frac{dn_{z+1}}{dt} = n_e n_z S(z,T_e) - n_e n_{z+1}\left[S(z+1,T_e) + \alpha_r(z+1,T_e) + n_e\alpha_{3b}(z+1,T_e)\right] + n_e n_{z+2}\left[\alpha_r(z+2,T_e) + n_e\alpha_{3b}(z+2,T_e)\right] \quad (7)$$

where n_z is the density of ion z, n_e the electron density, S, α_r, and $n_e\alpha_{3b}$ the collisional ionisation, radiative recombination, and three-body recombination rate coefficients, and T_e the electron temperature. The temperature is a function of the laser power density (or intensity Φ) and scales as $\Phi^{3/5}$.

The rate equations for the z coupled equations for each ion are determined from cross sections averaged over a free electron distribution function (assumed to be Maxwellian). The semi-empirical rate equations are a function of electron temperature T_e, electron density n_e , charge z, ionisation potential χ, and number of open shell electrons ξ. Dielectronic recombination is not included in this model, but can be included as a percentage of radiative recombination. The electron density is assumed to be equal to the critical electron density (or cut-off density), n_{ec}, where $n_{ec} \approx 10^{21}/\lambda^2$ cm^{-3} (λ in μm).

For a steady state model, $dn/dt = 0$, and thus the ratio of ionisation (S) and recombination processes (α_r and α_{3b}) is equal to the ion density from one ion stage to the next. n_{z+1}/n_z is a recursive relation, which when summed to 1 gives the fractional ion density (f_z) at each ion stage (z), and hence the ion distribution or average charge <z>.

$$f_z = \frac{n_{z+1}}{n_z} = \frac{S(z)}{\alpha_r(z+1) + n_e\alpha_{3b}(z+1)} \quad (7)$$

Figure 4 shows the ion density fractions for tin as a function of electron temperature to 100 eV for the Nd:YAG laser (λ = 1.064 μm) cut-off density of 9.843 x 10^{20} cm^{-3}. The open 4d-

subshell ions are indicated and are present from about 5–100 eV in varying fractions. Especially long plateaus correspond to noble gas-like species, for example Kr-like Sn XIV (Sn^{13+}), seen as the dominant species from about 50–70 eV. A range of ion stages are present in a plasma at any given electron temperature, where higher temperatures produce higher ion stages. Note that the dominant species at any temperature comprises about 40 to 50% of the total ion population.

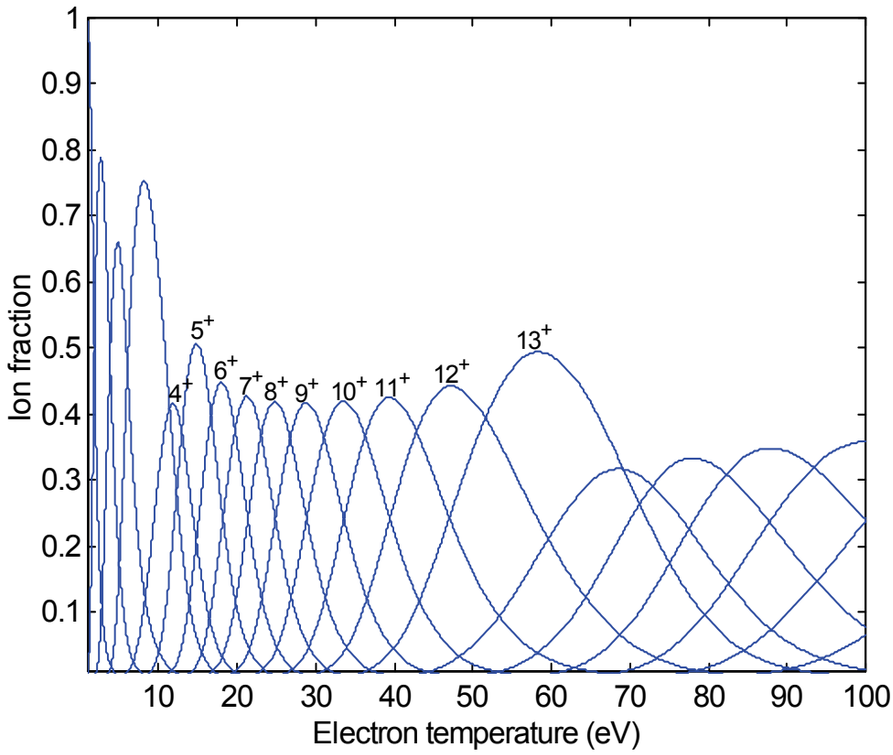

Fig. 4. Steady-state tin ion distribution, f_z, versus temperature (4d-subshell indicated)

To determine the ion distribution, the rate equations can also be solved using the simultaneous equation method (Cummings et al., 2004). This method is more general than the recursive relation method and can be used to include energy level populations within an ion stage, mixed ion species, and a time-dependent solution of the rate equations.

3.3 Steady-state source metric

A theoretical spectrum versus temperature and wavelength can be obtained using the statisitcal UTA as a function of wavelength and the ion fraction as a function of electron temperature, from which an intensity source metric (or figure of merit, F) can be calculated to quantify the in-band oscillator strength within the 2%, 13.5-nm bandwidth.

Figure 5 shows a continuous surface plot versus temperature (White et al., 2005), where the interacting 4d-4f and 4p-4d transitions overlap to form a broad UTA, which narrows with increasing temperature. The overall emission moves to shorter wavelength with temperature because of the higher contributing ion stages. The 4d-5p lines are seen at lower energies and lower temperatures until merging with the UTA. In an optically thick plasma, they will be relatively strong compared to the 4d-4f and 4p-4d lines which self absorb.

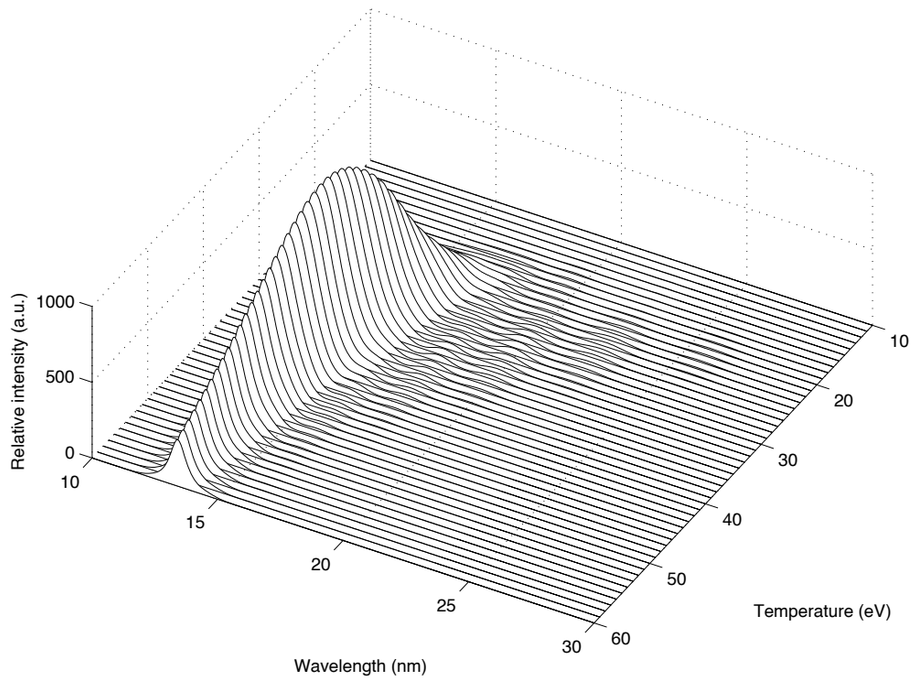

Fig. 5. Relative intensity versus temperature and wavelength

The source metric is taken as the product of the summed *gf* values for all transitions within each ion stage, weighted according to their distribution as a function of electron temperature with the multilayer mirror reflectivity (Eq. 9).

$$F = \sum_{\lambda} \sum_{z} R_{\lambda}^{n} f_z g f_{\lambda,z} \tag{9}$$

where R_λ is the wavelength-dependent reflectivity of the Mo/Si multilayer mirror, n is the number of mirrors, f_z is the fractional weighting of an ion of charge z, and $gf_{\lambda,z}$ is the weighted oscillator strength for that ion stage at a wavelength λ. F can be considered without the mirror reflectivity (*i.e.*, n = 0).

The calculated metric is shown over three wavelength ranges as a function of electron temperature (Figure 6) to highlight maximum emission as a function of wavelength (or atomic species). The relative in-band contribution increases and then decreases with temperature, showing the UTA diminishing as the 4d-subshell is fully stripped. Maximium 2% in-band emission is at approximately 40 eV. Note that the 7.4% range gives a simple estimate of out-of-band emission (OOB), known to reduce mirror lifetime because of thermal loading (Morris et al., 2007).

The results have been compared to experiment (White et al., 2005), where it is seen (Figure 7) that the long wavelength edge is matched at lower electron temperatures (and thus lower ion stages within the plasma) and the short wavelength edge matched at higher electron temperatures (and thus higher ion stages within the plasma).

Although a simplified UTA approach using a steady-state CR model gives important information about optimum plasma conditions in optically thin plasmas, the plasma is not wholly characterised by one temperature, and a more sophisticated spatially and temporally resolved model is required, that also includes radiation transport.

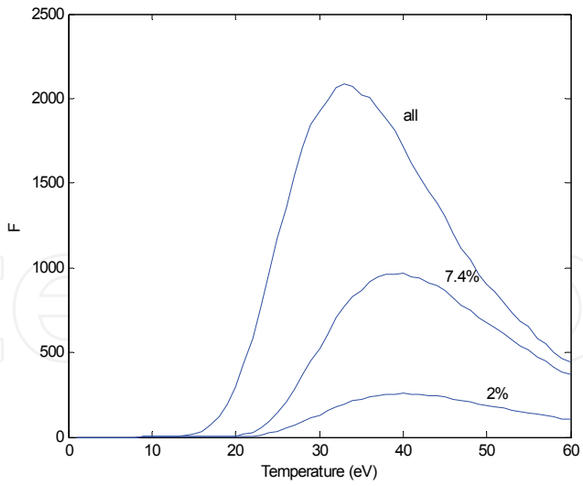

Fig. 6. Tin plasma figure of merit (2%, 7.4%, full spectral range) as a function of temperature

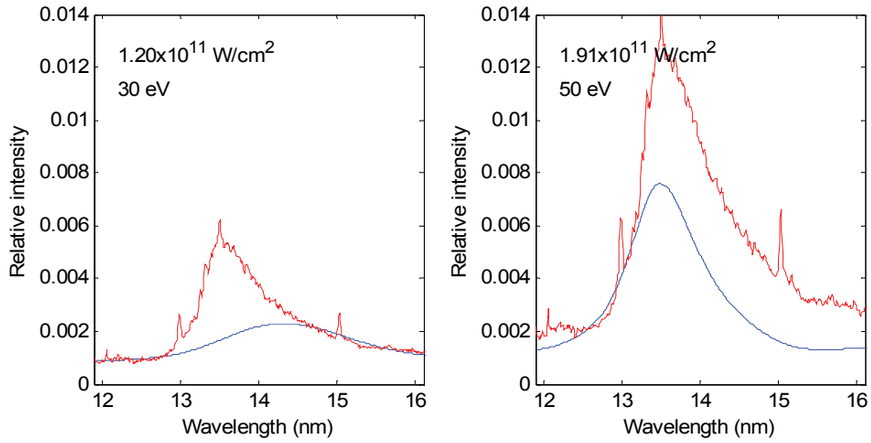

Fig. 7. Statistical UTA weighted by fractional ion density as a function of electron temperature (blue) and compared to experiment 6% tin-doped glass target (red)

3.4 Time-Dependent ion distribution and level populations

Hydrodynamic calculations are required to determine spatial and temporal electron temperature, electron density, ion distribution, and ultimately CE. The 1D Lagrangian, laser-plasma code MED103 (Christiansen et al., 1974) calculates density, velocity, ion temperature, electron temperature as functions of space and time, using the Navier-Stokes equations and can be readily coupled to an atomic model.

To illustrate the complex dynamics within the plasma, simulation results for a Nd:YAG, λ = 1064-nm, 15-ns (FWHM), Φ = 1.3 x 10^{11} W/cm^2 pulse on a solid tin cylindrical target (400 cells) are presented (Figure 8). The electron density (left) and electron temperature (right) versus distance at 3 times (top: before, at, and after the peak of the pulse), and versus time for 3 distances (bottom: at the plasma edge) are shown.

Here the overdense region (left), where the electron density varies from 10^{23} to 10^{19} cm^{-3} at the ablation front, and the effect of plasma heating (right) can be seen.

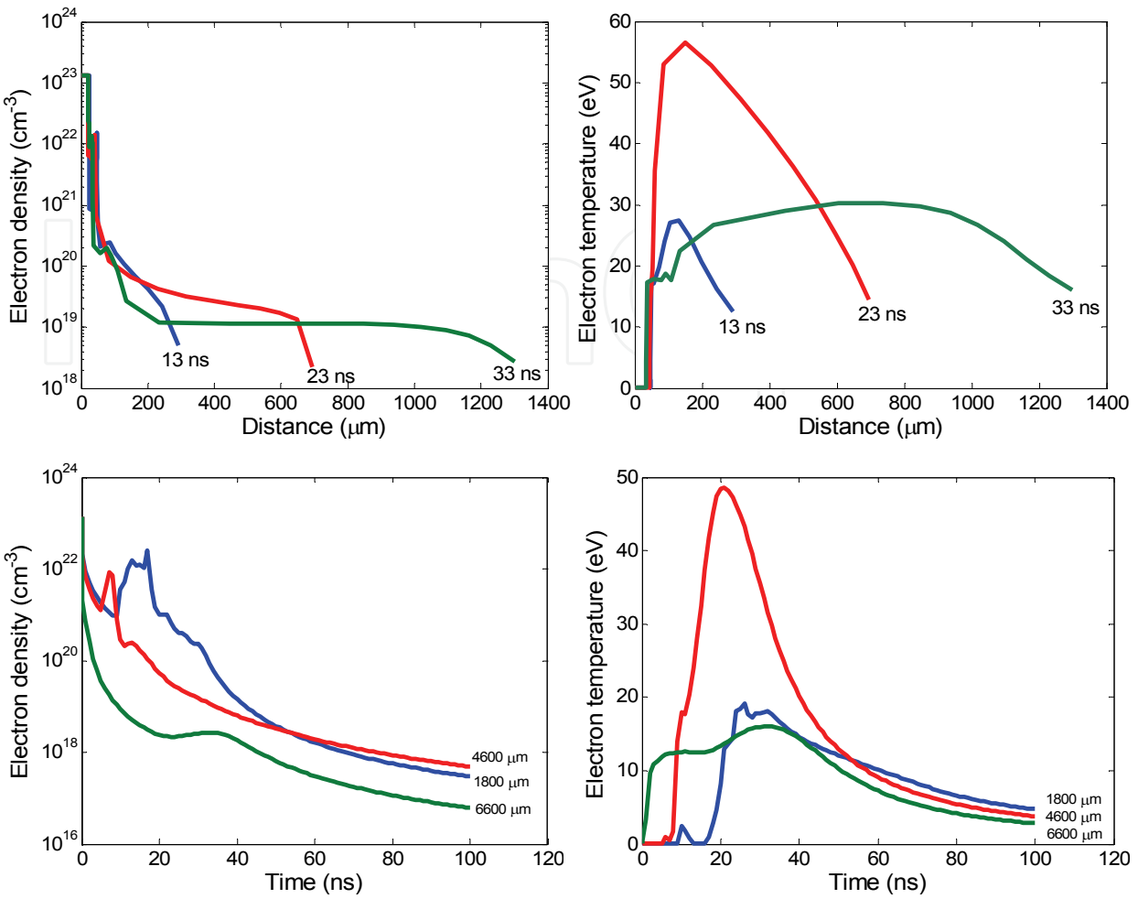

Fig. 8. Hydrodynamics versus space and time (Nd:YAG, 15 ns, .3 x 10^{11} W/cm^2 on solid tin)

Using the average atom (AA) model, the ion distribution and excited (*l*-degenerate) level populations are solved together with the plasma hydrodynamics, and the emission and absorption coefficients calculated independently in opacity tables. The AA model uses a statistical average over all ions to save computation (Djaoui & Rose, 1992), resulting in a fictitious ion with non-integer occupation numbers.

The statistical UTA representation (described above) and an energy functional methodology (Itoh et al., 1987) can be used to remove the *nl* degeneracy for $\Delta n = 0$ (4-4) transitions to calculate level populations required for radiation transport modeling (White et al., 2007). The screened hydrogenic model (More, 1982, Perrot, 1989) and UTA statistical data are used to interpolate between energy levels to calculate *nl*-splitting for 4-4 transitions.

Figure 9 shows the ion distribution (left) and a typical plot of population number density versus distance (right, ground state $4p^6 4d^N$ (black), and excited states, $4p^6 4d^{N-1} 4f^1$ (green), $4p^5 4d^{N+1}$ (blue), and $4p^6 4d^{N-1} 5p^1$ (red)) at the peak of the pulse (23 ns) for Sn X.

Note that all of the 4d-subshell ion fractions rise, fall, and rise with distance, showing the coupling to the laser pulse on the ablation front (left). Furthermore, the rise, fall and rise of the level populations (primarily a function of ion fraction) is more pronounced at the peak of the pulse as expected with increased coupling to the laser (right). Here, the increased $4p^5 4d^{N+1}$ (blue) and decreased $4p^6 4d^{N-1} 5p^1$ (red) populations are seen with increased

ionisation, indicating the increased 4p-4d and decreased 4d-5p contributions. Note the significant population decrease at the edge of the plasma (last cells).

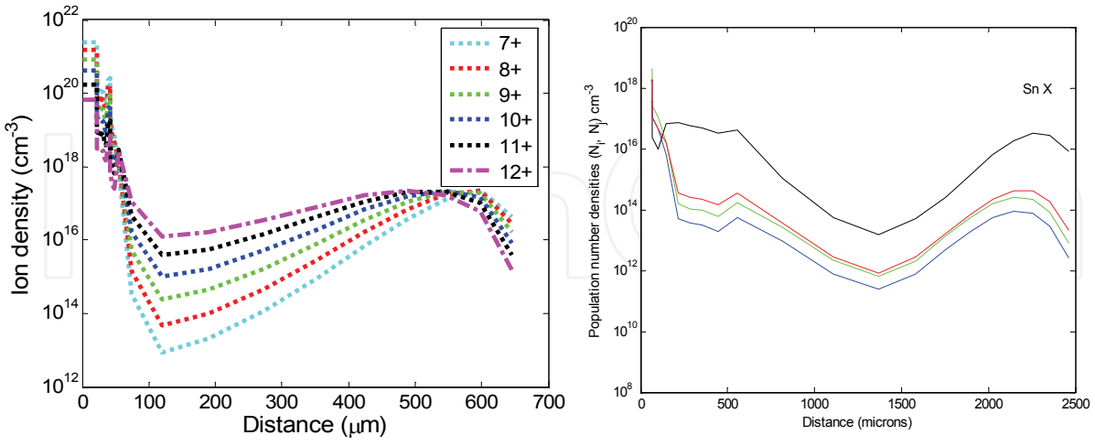

Fig. 9. Ion distribution (Sn^{6+} to Sn^{12+}) (left) and level populations at the peak of the pulse (Sn^{9+}) (right) versus distance

3.5 Radiation transport

The methodology for calculating radiation transport in an optically thick plasma is described elsewhere (Djaoui et al., 1994, Wark et al., 1995, Patel et al., 1997, White et al. 2009) and is summarised here. Radiation transfer involves absorption and emisison of spectral radiation along a path with differing hydrodynamic conditions, which can significantly alter the resultant spectra (line intensities and shape). The radiative transfer equation is given by

$$\frac{\partial I_\nu}{\partial z} = K_\nu I_\nu + E_\nu \tag{10}$$

where K_ν is the absorption coefficient, I_ν is the intensity, E_ν the total emissivity (all functions of frequency ν), and z the distance.

Eq. 10 is computationally intensive and thus an optical thickness, τ_ν, from the point of emission to the plasma boundary is defined to simplify (Djaoui et al., 1994). Thus

$$\frac{\partial I_\nu}{\partial \tau_\nu} = I_\nu - S_\nu \tag{11}$$

where I_ν is the radiation intensity, τ_ν the optical depth, and S_ν the source function, where $S_\nu = E_\nu / K_\nu$. (In the optically thick limit $\tau_\nu >> 1$, and in the optically thin limit $\tau_\nu << 1$.) The solution to the radiative transfer equation is given as

$$I_\nu(\tau_\nu) = I_\nu^0 e^{-\tau_\nu} + \int_0^{\tau_\nu} S_\nu(t) e^{-t} dt \tag{12}$$

where the integral is evaluated from τ_ν to the edge of the material and I_ν^0 is the incident radiation intensity at τ_ν.

For a homogeneous plasma with no incident radiation, the intensity is thus

$$I_m(\nu) = \sum_l S_m^l(\nu)[1 - \exp(\chi_m^l(\nu)\Delta z_m)] \tag{13}$$

where S^l_m (ν) is the source function and χ^l_m (ν) is the opacity of line l and cell m and Δz_m the length of cell m. The sum is taken over each line.
The source function at a given frequency, ν, for line l and cell m is

$$S_m^l(\nu) = \frac{2h\nu^3}{c^2} \frac{1}{\left[\frac{N_i g_j}{N_j g_i} - 1\right]} \tag{14}$$

where S is in W/m²/sr[/Hz/s], N_i and N_j are the population number densities in cm^{-3}, g_i and g_j are the degeneracies of the ith and jth levels (i lower level and j higher level).
The opacity for line l and cell m is

$$\chi_m^l(\nu) = \frac{\pi e^2}{4\pi\varepsilon_0 m_e c} f_{ij} N_i \left[1 - \frac{N_j g_i}{N_i g_j}\right] \phi_m^l(\nu) \tag{15}$$

where f_{ij} is the absorption oscillator strength and ϕ^l_m (ν) is the area normalised line profile assumed to be the same in emission and absorption (Djaoui et al., 1994).
The emission profile is then recursively attenuated through successive cells, where the observed emission from cell m is

$$I_m^{obs}(\nu) = I_m(\nu) \exp\left(\sum - \chi_n(\nu)\Delta z_n\right). \tag{16}$$

3.6 Laser-plasma simulations

Using the 1D model described above, maximum CE can be determined based on optimum laser parameters of power density and pulse duration. A cylindrical target of 90-μm radius is assumed in all simulations for an incident laser wavelength of 1064 nm (Nd:YAG). Results are compared to experiment (Hayden et al., 2006), where a 15-ns simulated pulse duration was chosen to compare to experiment on a pure tin slab target.
Two simulation surveys are discussed, that vary power density and pulse duration. Power density is varied from 0.5 to 1.5 x 10^{11} W/cm² with a 15-ns duration (FWHM), and, then, using the power density with the maximum CE in the first survey (0.8 x 10^{11} W/cm²), the pulse duration is varied from 7 to 40 ns. The conversion efficiency was calculated for each case and the optimum laser parameters determined (Table 2 and Table 3).
The results of the two surveys showed a maximum CE at 0.8 x 10^{11} W/cm² for a 10-ns pulse. Figure 10 shows a simulated and experimental spectra (Hayden et al., 2006) (left) for the maximum CE case and CE versus power density (right) for the 15-ns cases (A1-A9). The calculated results underestimate the experimental power density needed because of the absence of lateral expansion along the target in a 1D model, where the calculated plasma reaches optimum electron temperature (30–40 eV) at a lower power density because no energy is converted into lateral expansion (White et al. 2009).

Run	Duration (ns) FWHM	Power density (x 10^{11} W/cm^2)	CE (% per 2π sr)	max <z>
A1	15	0.5	1.03	8.6
A2	15	0.6	1.58	9.9
A3	15	0.7	2.01	11.1
A4	15	0.8	2.21	12.2
A5	15	0.9	2.16	13.2
A6	15	1.0	1.84	14.2
A7	15	1.1	1.48	15.1
A8	15	1.3	1.06	16.7
A9	15	1.5	0.92	18.7

Table 2. Power density survey: 0.5–1.5 x 10^{11} W/cm^2 at 15 ns

Run	Duration (ns) FWHM	Power density (x 10^{11} W/cm^2)	CE (% per 2π sr)	max <z>
B1	7	0.8	1.93	9.4
B2	10	0.8	2.29	11.2
B3	15	0.8	2.21	12.2
B4	20	0.8	1.71	13.6
B5	23	0.8	1.16	14.0
B6	30	0.8	0.51	14.5
B7	40	0.8	0.29	14.7

Table 3. Pulse duration survey: 7–40 ns (FWHM) at 0.8 x 10^{11} W/cm^2

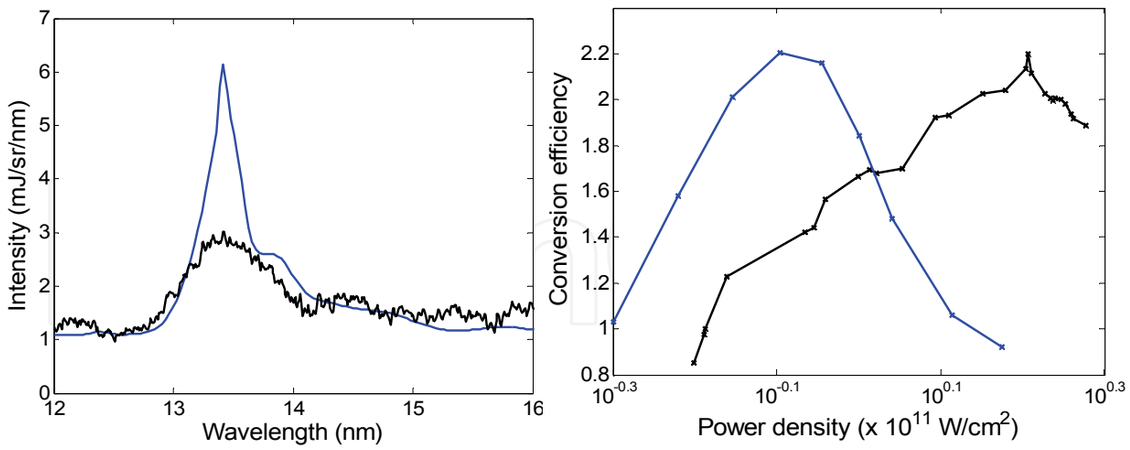

Fig. 10. In-band emission 1064 nm, 15 ns FWHM, 0.8 x 10^{11} W/cm^2 case (left) and conversion efficiency (right) versus laser power density (calculated (blue) and experiment (black))

3.7 The effect of laser pulse wavelength and pulse duration

The steady-state model can be used to compare the effect of wavelength of a Nd:YAG (1064 nm) which produces a critical electron density, n_{ec}, of 10^{21} cm^{-3}, and the 10,600-nm CO_2 (10

times the Nd:YAG wavelength) which produces a n_{ec} of 10^{19} cm^{-3} (1/100 that of Nd:YAG). The reduced electron density results in a greater average charge at the same electron temperature, because of the ion density dependence on three-body recombination, which decreases with decreased electron density (White et al., 2007). Using the ID model, a 2.2 times maximum CE was calculated for the CO_2 LPP at 7.2 x 10^8 W/cm^2 compared to that for the maximum Nd:YAG LPP CE at 3.3 x 10^{10} W/cm^2, in part because of reduced opacity in the more optically thin CO_2 plasma.

2D results using the RMHD code Z* highlight the effect of spatial pulse profile on opacity (White et al., 2008). Optimal in-band EUV emission occurs primarily from the plasma core (30-40 eV); however, core emission is reduced by self-absorption and absorption in the colder wings because of the high absorption cross section of lower stage ions (Lysaght et al., 2004). Figure 11 shows the larger hot core region for a flat-top spatial profile pulse (left) compared to a Gaussian spatial pulse (right), because of greater coupling.

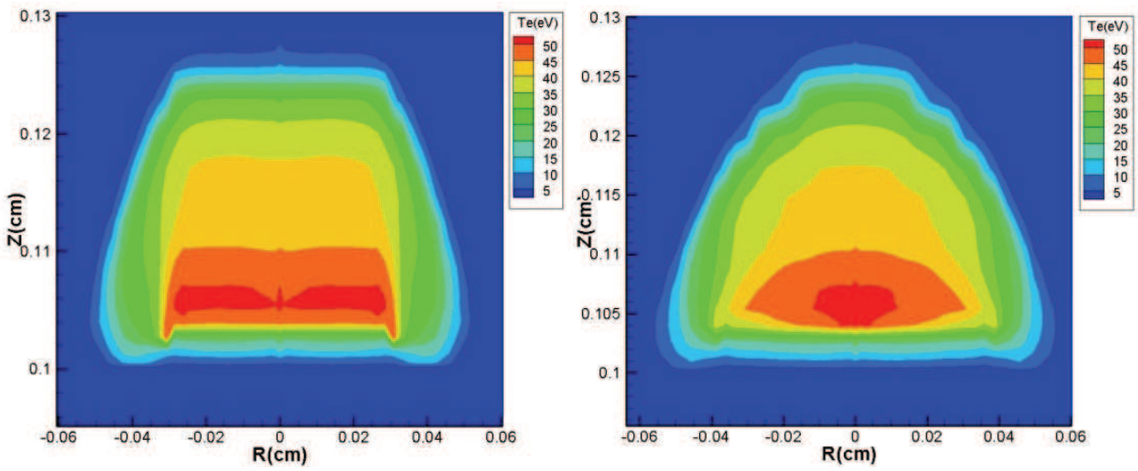

Fig. 11. Electron temperature flattop (left) and Gaussian (right) for a 2.2-ns Nd:YAG

4. Current trends and future challenges

Among the key challenges facing LPP EUV source optimisation are coupling the maximum amount of laser energy into the plasma, and maintaining the plasma in an emitting state for the maximum time possible for a given laser pulse duration. By using a pre-pulse (Dunne et al., 2000), it is possible to prepare a cool plasma on the surface of a solid target, with a density closer to the critical density, which is set by the wavelength of the main driving laser. Thus the bulk of the energy in the main laser pulse is coupled to the cool plasma, increasing the overall CE of the system. Parameters that can be varied include the wavelength of the two lasers, their pulse energies and durations, and the time delay between the two pulses. This latter parameter allows the pre-plasma to expand to the optimum size/density balance and a peak CE obtained at a well-defined delay (Higashiguchi et al., 2006, Ando et al., 2006). The pre-pulse-pulse approach is also valuable with droplet targets where the initial droplet density may be orders of magnitude in excess of the critical density corresponding to the main laser pulse.

A more complex approach involves the tailoring of the main laser pulse shape, away from a simple Gaussian to increase CE. Studies have shown (White et al., 2005) that a sharp fall in the laser pulse soon after the peak intensity can increase the CE, as the tail of the Gaussian pulse does not maintain the plasma at a sufficient temperature to emit EUV radiation, and hence is wasted. Experimental approaches include temporally multiplexing a number of Gaussians of different FWHM, to create a range of pulse shapes, perhaps using a learning algorithm and feedback to assist in the optimisation of the pulse shape. Using CO_2 lasers it is possible to control the pulse duration, and to an extent the pulse shape using a plasma shutter (Hurst & Harilal, 2009). It is simpler to multiplex Nd:YAG lasers, for example, by combining the beams in a single lens setup (Ellwi et al., 2005).

Intelligent algorithms may also be implemented to drive a plasma model, incorporating MHD, radiation transport and plasma expansion, to locate the ideal pulse shape in a complex multi-dimensional parameter space. Potential approaches from control theory include Swarm Intelligence, Multi Object Optimisation and Genetic Algorithms.

The use of large, multilayer, plasma-facing optics as collectors in systems with multi-kW plasma sources raises the issue of debris emission, which both sputters the surface of the mirror and deposits fuel debris on it, in each case degrading reflectivity (Srivastava et al., 2007). A range of mitigation measures has been proposed including magnetic fields, plasma shutters, buffer gases, sacrificial layers, and combinations of these. In addition, the reduction of debris emission by target design has resulted in the proposed use of mass-limited targets, targets containing nanoparticles (Kaku et al., 2008), cavity targets (Ueno et al., 2007), etc. However, it is most likely that a combination of these measures will be required in addition to a cleaning routine based on scavenger gases flushed through the system.

5. Conclusions

In this review, we have introduced computational methods for LPP modeling, and used both a simple, steady-state model in an optically thin plasma and a more sophisticated, 1D model with radiation transport in an optically thick plasma to illustrate a particular calculation. Optimum plasma conditions were estimated, e.g., electron temperature for maximum in-band emission (40 eV) as well as optimum laser parameters for maximum CE for a Nd:YAG LPP (0.8×10^{11} W/cm^2, 10-ns pulse). The effect of laser wavelength on CE was calculated using the steady-state model and the effect of spatial pulse shape using a 2D RMHD code.

The use of different codes is primarily a trade off between computation time and sophistication although complicated atomic theory involving hundreds of thousands of transitions can be investigated with simplified models to benchmark more sophisticated multi-dimensional codes. Much modeling work continues into the search for optimum laser parameters and plasma conditions necessary in HVM EUVL.

6. Acknowledgement

The authors wish to acknowledge support from Science Foundation Ireland under principal investigator grant 07/IN.1/B1771.

7. References

Al-Rabban, M., Richardson, M., Scott, H., Gilleron, F., Poirier, M., & Blenski, T., Modeling LPP sources, *EUV Sources for Lithography*, Ch. 10, Ed. V. Bakshi, SPIE Press (2005).

Ando, T., Fujioka, S., Nishimura, H., Ueda, N., Yasuda, Y., Nagai, K., Norimatsu, T., Murakami, M., Nishihara, K., Miyanaga, N., Izawa, Y., & Mima., K., Optimum laser pulse duration for efficient extreme ultraviolet light generation from laser-produced tin plasmas, *Appl. Phys. Lett.* 89, 151501 (2006).

Attwood, D., *Soft X-Rays and Extreme Ultraviolet Radiation, Principles and Applications*, University Press, Cambridge (1999).

Attwood, D., Extreme ultraviolet light sources for semiconductor manufacturing, *J. Phys. D* 37, 23 (2004).

Bar-Shalom, A., Oreg. J., & Klapisch, M., Collisional radiative model for heacy atoms in hot non-local-thermodynamical-equilibrium plasmas, *Phys. Rev. E* 56, 71–73 (1997).

Bar-Shalom, A., Klapisch, & M., Oreg. J., HULLAC, an integrated computer package for atomic processes in plasmas, *J. Quant. Spectrosc. Radiat. Transfer* 71, 169-188 (2001).

Bauche, J. & Bauche-Arnoult, C., Transition arrays in the spectra of ionised atoms, *Advances in atomic and molecular physics* 23, 131–195 (1988).

Bauche, J. & Bauche-Arnoult, C., Unresolved transition arrays, *Physica Scripta* 37, 659–663, (1988).

Bauche, J. & Bauche-Arnoult, C., Statistical approach to the spectra of plasmas, *Physica Scripta* T40, 58–64 (1992).

Carroll, P.K. & Kennedy, E.T., Laser-produced plasmas, *Contemporary Physics*, 22, 1, 61–96 (1981).

Christiansen, J.P., Ashby, D.E.T.F., & Roberts, K.V., Medusa: a one-dimensional laser fusion code, *Comput. Phys. Commun.* 7, 271–287 (1974).

Christiansen & Winsor, CASTOR 2: a two-dimensional laser target code, *Comput. Phys. Commun.* 17, 397 (1979).

Chung, H.-K., Chen, M.H., Morgan, W.L., Ralchenko, Y., & Lee, R.W., FLYCHK: Generalized population kinetics and spectral model for rapid spectroscopic analysis for all elements, *High Energy Density Physics* 1, 3–12 (2005).

Colombant & Tonon, X-ray emission in laser produced plasmas, *J. Appl. Phys.* 44, 8, 3524 (1973).

Cowan, D., *The theory of atomic structure and spectra*, University of California Press, Berkeley (1981).

Cummings, A., O'Sullivan, G., Dunne, P., Sokell, E., Murphy, N., White, J., Fahy, K., Fitzpatrick, A., Gaynor, L., Hayden, P., Kedzierski, D., Kilbane, D., Lysaght, M., McKinney, L., & Sheridan, P., Variable composition laser-produced Sn plasmas—a study of their time-independent ion distributions, *J. Phys. D* 37, 2376–2384 (2004).

Derra, G., Zink, P., Krücken, T., Weber, A. & Pankert, J., Tin delivery systems for gas discharge sources, *EUV Source Workshop*, San Jose, CA, USA (2005).

Djaoui, A., Rose, S.J., & Wark, J.S., Calculation of the effects of velocity gradients and opacity on line transfer in laser-produced plasmas, *J. Quant. Spect. Radiat. Trans.* 52, 5, 531 (1994).

Dunne, P., O'Sullivan, G., & O'Reilly, D., Prepulse-enhanced narrow bandwidth soft x-ray emission from a low debris, subnanosecond, laser plasma source, *Appl. Phys. Lett*. 76, 1, 34-36 (2000).

Dusterer, S., Schoerer, H., Ziegler, W., Ziener, C., & Sauebrey, R., Optimization of EUV radiation yield from laser-produced plasma, *Applied Physics B* 73, 693–698 (2001).

Ellwi, S., Comley, A., Hay, N., Henderson I., & Brownell, M., Proc. SPIE, 5751, 272 (2005).

Fujioka, S., Nishimura, H., Nishihara, K., Sasaki, A., Sunahara, A., Okuno, T., Ueda, N., Ando, T., Tao, Y., Shimada, Y., Hashimoto, K., Yamaura, M., Shigemori, K., Nakai, M., Nagai, K., Norimatsu, T., Nishikawa, T., Miyanaga, N., Izawa, Y., & Mima, K., Opacity effect on extreme ultraviolet radiation from laser-produced tin plasmas, *Phys. Rev. Lett*. 95, 235004 (2005).

Fujioka, S., Shimomura, M., Shimada, Y., Maeda, S., Sakaguchi, H., Nakai, Y., Aota, T., Nishimura, H., Ozaki, N., Sunahara, A., Nishihara, K., Miyanaga, N., Izawa, Y., & Mima, K., Pure-tin microdroplets irradiated with double laser pulses for efficient and minimum-mass extreme-ultraviolet light source production, *Appl. Phys. Lett.* 92, 241502 (2008a).

Fujioka, S., Nishimura, H., Shimomura, M., Sakaguchi, H., Nakai, Y., Aota, T., Shimada, Y., Sunahara, A., Nishihara, K., Optimum Laser-Produced Plasma for Extreme Ultraviolet Light Source, Journal of Physics: Conference Series 112 042049 (2008b).

Grant, I.P., McKenzie, B.J., Norrington, P.H., Mayers, D.F. & Pyper, N.C., An atomic multiconfigurational Dirac-Fock package, *Comput. Phys. Commun*. 21, 207–31 (1980).

Greim, H. R., *Plasma Spectroscopy*, McGraw-Hill, New York (1964).

Gumbrell, E. T., Smith, R. A., Ditmire, T., Djaoui, A., Rose, S. J., & Hutchinson, M. H. R., Picosecond optical probing of ultrafast energy transport in short pulse laser solid target interaction experiments, Physics of Plasmas 5, 3714 (1998).

Gu, M. F., *Astrophysical Journal*, 582, 1241, 2003.

Hayden, P., Cummings, A., Murphy, N., O'Sullivan, G., Sheridan, P., White, J. & Dunne, P., 13.5 nm extreme ultraviolet emission from tin based laser plasma sources*, J Appl Phys*. 99, 093302 (2006).

Higashiguchi, T., Kawasaki, K., Sasaki, W., Kubodera, S., Enhancement of extreme ultraviolet emission from a lithium plasma by use of dual laser pulses, *Appl. Phys. Lett*. 88, 161502 (2006).

Hurst, N. & Harilal, S. S., Pulse shaping of transversely excited atmospheric CO_2 laser using a simple plasma shutter, *Rev. Sci. Instrum.* 80, 035101 (2009).

Itoh, M., Yabe, T., & Kiyokawa, S., Collisonal-radiative and average-ion hybrid models for atomic processes in high-Z plasmas, *Phys. Rev. A* 35, 233 (1987).

International technology roadmap for semiconductors: http://public.itrs.net.

Jin, F. & Richardson, M., New laser plasma source for extreme-ultraviolet lithography, *Appl. Opt*. 34, 5750–5760 (1995).

Kaku, M., Suetake, S., Senba, Y., Kubodera, S., Katto, M., & Higashiguchi, T., Deposited debris characteristics and its reduction of a laser-produced plasma extreme ultraviolet source using a colloidal tin dioxide jet target, *Appl. Phys. Lett*. 92, 181503 (2008).

Key, M. H. & Hutcheon, R. J., Spectroscopy of laser-produced plasmas, *Advances in Atomic and Molecular Physics* 16, Ed. Bates, Sir David, Academic Press (1980).

Lysaght, M., Kilbane, D., Murphy, N., Cummings, A., Dunne, P. & O'Sullivan, G., Opacity of neutral and low ion stages of Sn at the wavelength 13.5 nm used in extreme-ultraviolet lithography, *Phys. Rev. A* 72, 014502 (2005).

MacFarlane, J.J., Rettig, C.L., Wang, P., Golovkin, I.E., and Woodruff, P.R., Radiation-hydrodynamics, spectral, and atomic physics modeling of laser-produced plasma euv lithography light sources, in *Emerging Lithographic Technologies IX*, Proc. SPIE, Ed. R.S. Mackay, 5751, 588–600 (2005).

Mandelbaum, P., Finkenthal, M., Schwob, J.L., & Klapisch, M., Interpretation of the quasicontinuum band emitted by highly ionized rare-earth elements in the 70–100 Å range, *Phys. Rev. A* 35, 12, 5051–5059 (1987).

Mirone, A., Gauthier, J. C., Gilleron, F., & Chenais-Popovics, C., Non-LTE opacity calculations with *n-l* splitting for radiative hydrodynamic codes, *J. Quant. Spectrosc. Radiat. Transfer* 27, 3, 345–357 (1982).

More, R. M., Electronic energy-levels in dense plasmas, *J. Quant. Spectrosc. Radiat. Transfer* 58, 791–802 (1997).

Morris, O., Hayden, P., O'Reilly, F., Murphy, N., & Dunne, P., Angle-resolved absolute out-of-band radiation studies of a tin-based laser-produced plasma source, *Appl. Phys. Lett.*, 91, 081506 (2007).

Nishikawa, T., Takabe, H., & Mima, K., Atomic modeling and radiation transport in laser produced plasmas, in *Technology Reports of the Osaka University* 41, 2059, 253–266 (1991).

O'Sullivan, G. & Carroll, P. K., 4d–4f emission resonances in laser-produced plasmas, *J. Opt. Soc. Am* 71, 3, 227–230 (1981).

O'Sullivan, G. & Faulkner, R., Tunable narrowband soft x-ray source for projection lithography, *Opt. Eng.* 33, 3978 (1994).

Patel, P.K., Wark, J.S., Heading, D.J., Djaoui, A., Rose, S.J., Renner, O., & Hauer, A., Simulation of x-ray line transfer in a cylindrically expanding plasma *J. Quant. Spect. Radiat. Trans.* 57, 683 (1997).

Perrot, F., Fast calculation of electronic structure in plasmas: the screened hydrogenic model with *l*-splitting, *Physica Scripta* 39, 332–337 (1989).

Peyrusse, O., Atomic configuration averages and nonlocal thermodynamical equilibrium plasma spectroscopy calculations, *J. Phys. B: At. Mol. Opt. Phys.* 32, 683-700 (1999).

Rollinger, B., Bleiner, D., Chokani, N. & Abhari, R.S., Characteristics of a minimum-debris optimum conversion efficiency tin-based LPP source, in *Emerging Lithographic Technologies XII*, Proc. SPIE, Ed. F.M. Schellenberg, 6921, 1–12 (2008).

Sasaki, A., Nishihara, K., Koike, F., Kagawa, T., Nishikawa, T., Fujima, K., Kawamura, T. & Furukawa, H., Simulation of the EUV spectrum of Xe and Sn plasmas, *J. Sel. Top. Quant. Elec.* 10, 1307 (2004).

Salzmann, D., *Atomic physics in hot plasmas*, International series of monographs on physics, Oxford University Press (1998).

Sequoia, K.L., Tao, Y., Yuspeh, S., Burdt, R., & Tillack, M.S., Two dimensional expansion effects on angular distribution of 13.5 nm in-band extreme ultraviolet emission from laser-produced Sn plasma, *Appl. Phys. Lett*. 92, 221505 (2008).

Shimada, Y., Nishimura, H., Nakai, M., Hashimoto, K., Yamaura, M., Tao, Y., Shigemori, K., Okuno, T., Nishihara, K., Kawamura, T., Sunahara, A., Nishikawa, T., Sasaki, A., Nagai, K., Norimatsu, T., Fujioka, S., Uchida, S., Miyanaga, N., Izawa, Y., & Yamanaka, C., Characterization of extreme ultraviolet emission from laser-produced spherical tin plasma generated with multiple laser beams, *Appl. Phys. Lett*. 86, 051501 (2005).

Sondhauss, P., Rose, S. J., Lee, R. W., Al'miev, I., & Wark, J. S., Extension of the code suite FLY to a multi-cell postprocessor for hydrodynamics plasma simulation codes, *J. Quant. Spectrosc. Radiat. Transfer* 71, 721-728 (2001).

Srivastava, S.N., Thompson, K. C., Antonsen, E. L. Qiu, H., Spencer, J. B., Papke, D., & Ruzic, D. N., Lifetime measurements on collector optics from Xe and Sn extreme ultraviolet sources, *J. Appl. Phys*. 102, 023301 (2007).

Svendsen, W. & O'Sullivan, G., Statistics and characteristics of XUV transition arrays from laser-produced plasmas of the elements tin through iodine, *Physical Review A: General Physics* 50, 5, 3710–3718 (1994).

Tao, Y., Nishimura, H., Okuno, T., Fujioka, S., Ueda, N., Nakai, M., Nagai, K., Norimatsu, T., Miyanaga, N., Nishihara, K., Izawa, Y., & Izawa, Y., Characterization of denisty profile of laser-produced Sn plasma for 13.5 nm extreme ultraviolet source, *Appl. Phys. Lett*. 87, 241502 (2005).

Takahashi, A., Nakamura, D., Tamaru, K., Akiyama, T., & Okada, T., Emission characteristics of debris from CO2 and Nd:YAG laser-produced tin plasmas for extreme ultraviolet lithography light source, *Appl. Phys. B* 92, 73–77 (2008).

Ueno, Y., Soumagne, G., Sumitani, A., Endo, A., & Higashiguchi, T., Enhancement of extreme ultraviolet emission from a CO2 laser-produced Sn plasma using a cavity target, *Appl. Phys. Lett*. 91, 231501 (2007).

Wark, J.S., Renner, O, Djaoui, A., Rose, S. J., Missalla, T., Neely, D., Foerster, E., & Hauer, A., Measurements and simulation of the intensity and shape of the hydrogenic Al resonance line ($1s^2S$-$2p^2P$) in laser-produced plasmas *J. Quant. Spectrosc. Radiat. Transfer* 54, 1/2, 419 (1995).

White, J., Hayden, P., Dunne, P., Cummings, A., Murphy, N., Sheridan, P., & O'Sullivan, G., Simplified modeling of 13.5 nm unresolved transition array emission of a Sn plasma and comparison with experiment, *J. Appl. Phys*. 98, 113301 (2005).

White, J., Dunne, P., Hayden, P., O'Reilly, F., & O'Sullivan, G. Optimizing 13.5 nm laser-produced tin plasma emission as a function of laser wavelength, *Appl. Phys. Lett*. 90, 181502 (2007).

White, J., Dunne, P., Hayden, P., & O'Sullivan, G. Simplified one-dimensional calculation of 13.5 nm emission in a tin plasma including radiation transport, *Appl. Phys. Lett*. **106**, 113303 (2009).

White, J., O'Sullivan, G., Zakharov, S., Choi, P., Zakharov, V., Nishimura, H., Fujioka, S., & Nishihara, K., Tin laser-produced plasma source modeling at 13.5 nm for extreme ultraviolet lithography, *Appl. Phys. Lett*. 92, 151501 (2008).

Yamuara, M, Uchida, S., Sunahara, A., Shimada Y., Nishimura, H., Fujioka, S., Okuno, T., Hashimoto, K., Nagai, K., Norimatsu, T., Nishihara, K., Miyanga, N., Izawa, Y., & Yamanaka, C., Characterization of extreme ultraviolet emission using the fourth harmonic of a Nd:YAG laser, *Appl. Phys. Lett.* 86, 181107 (2005).

Zakharov, S.V., Novikov, V.G., Choi, P., Z* Code for DPP & LPP source modeling, *EUV Sources for Lithography,* Ch. 8, Ed. V. Bakshi, SPIE Press (2005).

Zimmerman, G.B. & Kruer, W.L., Numerical simulation of laser-initiated fusion, *Comments Plasma Phys. Control. Fusion* 2, 51–61 (1975).

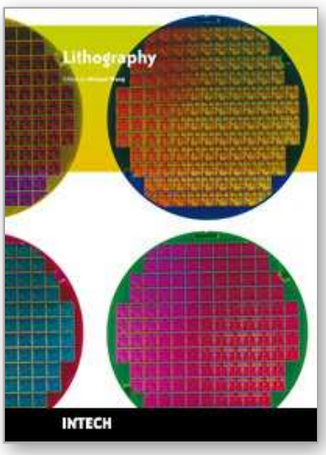

Lithography

Edited by Michael Wang

ISBN 978-953-307-064-3

Hard cover, 656 pages

Publisher InTech

Published online 01, February, 2010

Published in print edition February, 2010

Lithography, the fundamental fabrication process of semiconductor devices, plays a critical role in micro- and nano-fabrications and the revolution in high density integrated circuits. This book is the result of inspirations and contributions from many researchers worldwide. Although the inclusion of the book chapters may not be a complete representation of all lithographic arts, it does represent a good collection of contributions in this field. We hope readers will enjoy reading the book as much as we have enjoyed bringing it together. We would like to thank all contributors and authors of this book.

How to reference

In order to correctly reference this scholarly work, feel free to copy and paste the following:

White, Dunne, and O'Sullivan (2010). Steady-State and Time-Dependent LPP Modeling, Lithography, Michael Wang (Ed.), ISBN: 978-953-307-064-3, InTech, Available from: http://www.intechopen.com/books/lithography/steady-state-and-time-dependent-lpp-modeling

INTECH
open science | open minds

InTech Europe

University Campus STeP Ri
Slavka Krautzeka 83/A
51000 Rijeka, Croatia
Phone: +385 (51) 770 447
Fax: +385 (51) 686 166
www.intechopen.com

InTech China

Unit 405, Office Block, Hotel Equatorial Shanghai
No.65, Yan An Road (West), Shanghai, 200040, China
中国上海市延安西路65号上海国际贵都大饭店办公楼405单元
Phone: +86-21-62489820
Fax: +86-21-62489821

IntechOpen